diffusion-fundamentals.org

The Open-Access Journal for the Basic Principles of Diffusion Theory, Experiment and Application

Driven diffusion in nanoscaled materials

Tony Albers[1], Michael Bauer[1], Christian von Borczyskowski[1], Frank Gerlach[1,3], Mario Heidernätsch[1], Jörg Kärger[2], Daria Kondrashova[2], Günter Radons[1#], Sebastian Schubert[1,4], Alexander Shakhov[2], Daniela Täuber[1,5], Rustem Valiullin[2§], Philipp Zeigermann[2]*

[1]Institute of Physics, Technische Universität Chemnitz, Chemnitz, Germany

[2]Institute for Experimental Physics I, Universität Leipzig, Leipzig, Germany

[3]now at Fibotec Fiberoptics GmbH, Meiningen, Germany

[4]now at MPI for Biophysical Chemistry, Göttingen, Germany

[5]now at Lund University, Lund, Sweden

*borczyskowski@physik.tu-chemnitz.de, [#]radons@physik.tu-chemnitz.de,

[§]valiullin@uni-leipzig.de

Abstract

Mass transfer processes in which specific interactions with environments lead to complex diffusion patterns, such as the occurrence of transient sub-diffusive behaviors or of heterogeneous diffusion, were studied by means of two different experimental techniques, namely single-particle tracking operating with single molecules and nuclear magnetic resonance operating with large molecular ensembles. As an important point, the combined application of these techniques allowed for a deeper insight into the microscopic diffusion mechanism in such complex systems, including those with broken ergodicity.

Particle tracking concentrated on the “Influence of substrate surface properties on heterogeneous diffusion of probe molecules in ultrathin liquid films”. The mobility of liquids at solid-liquid interfaces is influenced by substrate heterogeneities. Here we study the distribution of surface silanols on differently treated silicon wafers with thermal oxide by confocal florescence microscopy of adsorbed Rhodamine G molecules. We further investigate the influence of the substrate properties on probe molecule diffusion in ultrathin liquid TEHOS films by single molecule tracking. The results are compared to simulations of two-layer diffusion employing heterogeneous substrates.

Nuclear magnetic resonance has been applied to study translational diffusion of small organic molecules in nanopores and of polymer globules in the presence of larger polymer species. In both cases, the experiments revealed the occurrence of normal diffusion on the time scale of NMR experiments from ten to hundreds of milliseconds. While single particle tracking revealed the identical diffusivities for the former case, thus experimentally confirming the validity of the ergodicity theorem for diffusion, the discrepancies were noted for the latter case. More complex behavior revealing non-ergodic

diffusion-fundamentals.org 23 (2015) 3, pp 1–25

behavior for propagation of solid-liquid interfaces in disordered nanopores has further been studied using nuclear magnetic resonance cryoporometry.

A common basis for comparing and analyzing the experimental observables accessed by the two methods is the distribution of diffusivities, which provides the probability of observing a given diffusivity fluctuation along a trajectory or in an ensemble. An overview of its properties is given and the advantages in analyzing heterogeneous, anisotropic, or anomalous diffusion processes are elaborated.

Keywords: Surface silanols, ultrathin liquid films, single molecule detection, tracer diffusion, NMR, solid-liquid interface, simulation, distribution of diffusivities, heterogeneous diffusion, anisotropy, ergodicity

1 Influence of substrate surface properties on heterogeneous diffusion of probe molecules in ultrathin liquid films

1.1 Introduction

The mobility of liquids at solid-liquid interfaces is influenced by substrate heterogeneities. Here we study the distribution of surface silanols on differently treated silicon wafers with thermal oxide by confocal fluorescence microscopy of adsorbed Rhodamine G molecules. Silicon wafers with native or thermal oxide are widely used in technical applications, for example in solar cells or for chip fabrication [1]. The performance of such devices is influenced by surface chemistry [2] and by local interface properties [3]. In particular, silica surfaces are covered by hydroxyl groups (silanols) and water, depending on fabrication and temperature treatment [4, 5]. Due to the high fabrication temperature (1000 °C) of the thermal oxide, the silanol coverage is significantly lower compared to fumed silica [5]. Yet, the amount and distribution of surface silanols is known to affect nanotechnical fabrication routines, for example nanolithography [6] and coatings with self-assembled monolayers [7]. However, up to now only average silanol coverages were known from ensemble measurements on macroscopic scales [4]. Here we use laser scanning confocal microscopy to investigate the distribution of fluorescent rhodamine 6G (R6G) adsorbed on 100 nm thermal oxide of Si wafers. According to Iler [8] charged dye molecules preferentially physisorb to surface silanols. Thus, the derived spatial distribution of adsorbed R6G molecules unravels the distribution of surface silanols on a submicron range.

Interactions at solid-liquid interfaces influence dynamic properties of fluids [9, 10] and guest molecules therein, which in particular plays a role in surface processes [11]. Optical investigation of single molecule diffusion in ultrathin liquid films on quartz cover slips revealed anisotropic diffusion of probe molecules [12]. This has been related to liquid layering at solid-liquid interfaces [13, 14]. On the other hand, also heterogeneous interface chemistry and morphology causes anisotropies in probe molecule diffusion, see for example Figure 1 [15], showing trajectories with position related heterogeneities obtained from diffusing Rhodamine B (RhB) molecules in ultrathin TEHOS films on silicon substrates with 100 nm thermally grown SiO_2.

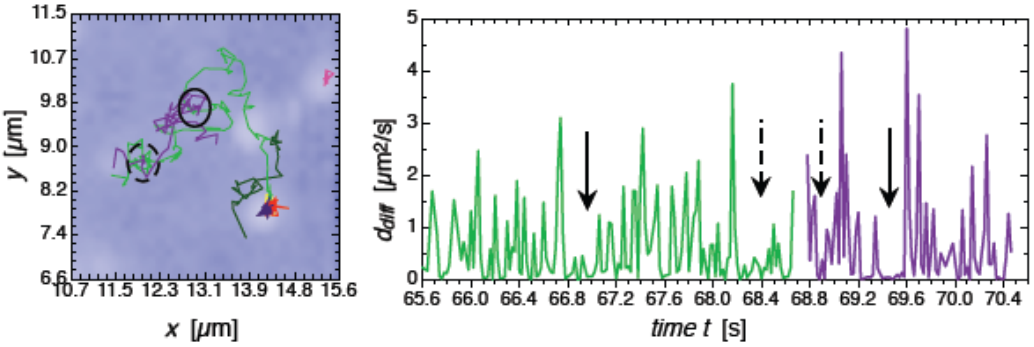

Figure 1: (left) Spatial plot of several immobile (bright areas) and three mobile (colored trajectories) obtained for a 10 nm thick TEHOS film on SiO_2 doped with RhB. (right) Diffusivities d_{diff} over total time t for light green and purple trajectory from the left image. The center of the solid and dashed circles in the left image mark areas with repeated periods of immobilization. The corresponding sets of periods are marked by solid and dashed arrows in the right image [15].

We use a homebuilt wide-field microscope [15] to study the influence of surface silanols on tracer diffusion in ultrathin liquid films. A common way to analyze diffusion experiments is to calculate mean square displacements (MSD) along detected trajectories [16]. However, long trajectories are necessary for good statistics [17]. In particular, heterogeneous or anomalous diffusion may be concealed due to the strong time averaging [18]. Moreover, the length of observed trajectories of single dye molecules is often limited by photobleaching and fluorescence intermittency [19]. Improved statistics can be achieved by detecting square displacements $(\Delta r)^2$ for succeeding time steps at a fixed time lag τ [20]. Thus, probability distributions $C(D)_\tau$ of time scaled $(\Delta r)^2$ between succeeding steps (diffusivities $d_{\mathrm{diff}} = (\Delta r)^2/(4\tau)$) provide a promising alternative [15, 21], since time averaging is realized and statistics are increased. $C(D)_\tau$ is defined as the probability of finding a diffusivity $d_{\mathrm{diff}} > D$. By scaling the squared displacements by the corresponding time lag τ, the trivial dependence on τ is removed and thus facilitates the comparability for different τ. However, for heterogeneous diffusion the shape of the probability distribution of diffusivities may still depend on τ [22]. For this reason, τ is noted as index. In case of homogeneous diffusion with diffusion coefficient D, the cumulative probability distribution of diffusivities amounts to

$$C(D)_\tau = \exp(-D/D_0). \tag{1}$$

In this case, probability distributions of diffusivities show a linear behavior in semi-log plots. In case of heterogeneous or anomalous diffusion, deviations from the mono-exponential function will appear. The further analysis then depends on the origin of such deviations [22].

Our findings show that the most regular distribution of surface silanols is obtained after etching the substrates in H_2O_2:H_2SO_4 (piranha) solution. Larger silanol clusters (on hydroxylated substrates) and larger distances between clusters (on tempered substrates) both enhance the heterogeneity of probe molecule diffusion.

1.2 Experimental

Si(100) wafers with 100 nm thermal oxide (dry O_2/HCl processed at 1000 °C) were obtained from the Center for Microtechnologies (ZfM, Chemnitz, Germany). In particular, for optical single molecule

investigations clean substrates are needed. In addition to commonly applied cleaning procedures [15], some substrates were boiled in ultraclean water for 20 h (“hydroxylated”), while others were tempered for 0.5 h at 800 °C in air (“tempered”). Substrates which underwent no additional treatment besides cleaning were used for comparison (“piranha”).

1.2.1 Determination of local silanol densities

The substrates were dipcoated in solutions of 10^{-6} mol/l Rhodamine 6G (R6G, Radiant Dyes) in ethanol using a stand-alone dipcoater (KSV-DX2, KSV Instruments). Similar concentrated solutions of R6G in toluene and in n-hexane were used for comparison (all solvents of spectroscopic grade, Merck). The withdrawal speed was 5 mm/min. Thereby a thin film of the solution is generated on the substrate. This film evaporates within 30 minutes, while dye molecules remain on the substrate at silanol binding sites. Fluorescence images of the R6G distribution were recorded with a homebuilt laser scanning confocal microscope [23]. Confocal images (100 ± 20 µm^2) were analyzed using WSxM 5.0 [24]. First, an intensity threshold was set for each image at its mean intensity minus one standard deviation. Then the images were smoothed with a Gaussian profile. From the processed images cluster sizes and coverages were determined using a cluster threshold size of 0.05 µm^2 [15, 25].

1.2.2 Probe diffusion measurements

Probe molecule diffusion at the solid liquid interface was investigated using ultrathin liquid films of Tetrakis-2-ethylhexoxy-silane (TEHOS, abcr). Due to the small film thickness of 5 ± 1 nm probe molecules remain close to the substrate. TEHOS films were obtained by dipcoating the substrates in solutions of few ppt TEHOS in n-hexane (spectroscopic grade, Merck) [15]. The solutions were doped with fluorescent Rhodamine B (RhB) resulting in a nanomolar concentration of dye molecules in the TEHOS film. The diffusion of RhB was recorded with a wide-field microscope with epi-illumination [15]. Since the z-focus (about 1 µm) is considerably larger than the film thickness, the 3D motion is projected onto a 2D motion parallel to the substrate. Thus, the obtained diffusion coefficients are effective diffusion coefficients parallel to the substrate. Series of 1800 succeeding images were recorded with a CCD camera (iXon DU 885K, Andor) at a frame rate of 1 fps, resulting in 30 min observation time for each measurement. The diffusion tracks were analyzed using home-written C/C++ programs [15, 26]. Immobile RhB molecules were excluded from further analysis.

1.3 Results and Discussion

1.3.1 Variation of Hydroxylation

Fluorescence intensities from R6G after evaporation of the solvent show an inhomogeneous distribution. In Figure 2 fluorescence intensities from three differently treated substrates are shown after evaporation of ethanol. Raw images have been processed with WSxM 5.0 [24]. Similar results were obtained using toluene and n-hexane as solvents (not shown). Thus, the distribution of R6G molecules on the thermal oxide is not influenced by the kind of solvent, but is determined by the properties of the substrate surface.

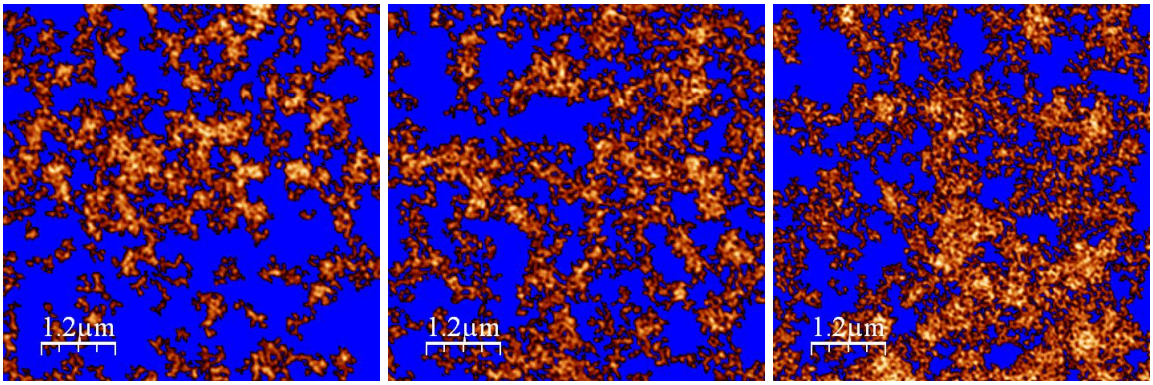

Figure 2: Clustered distribution of R6G fluorescence intensities on thermal SiO_2 after (left) tempering at 800 °C in air, (middle) cleaning in piranha with no further treatment, and (right) hydroxylation in water.

The results from image processing are given in Table 1. As can be seen, there is only a slight modification of the silanol coverage from 46.4 % for the tempered substrate to 53.5 % for the hydroxylated substrate. The largest average cluster size (1.97 ± 0.5 µm^2) is observed for the hydroxylated substrate. The thermal oxide tempered for 30 min at 800 °C shows only a slightly smaller average cluster size (1.42 ± 0.3 µm^2), while the smallest average cluster size (0.64 ± 0.2 µm^2), is obtained for the substrate which was etched in piranha followed by no further treatment. Hydroxylation increases the size of the silanol clusters, while the nearest neighbor distance between clusters remains at a similar value (0.66 ± 0.3 µm) as for the substrate after piranha treatment (0.64 ± 0.2 µm). Tempering the thermal oxide at high temperatures reduces primarily the amount of smaller clusters, thus leading to a threefold nearest neighbor distance (1.75 ± 0.5 µm) as compared to the other substrate treatments. This finding is in agreement with the assumption that surface silanols are preferentially generated and diminished at the edge of existing silanol clusters [4, 8]. The most regular distribution of surface silanols on thermal SiO_2 is achieved by etching in piranha, because the etching not only influences the density of surface silanols, but also affects the underlying SiO_2.

Substrate treatment	**tempered**	**piranha**	**hydroxylated**
Investigated area [µm^2]	110	110	81
# of clusters in area	36	85	22
Coverage [%]	46.4	49.4	53.5
Average cluster size and standard deviation [µm^2]	1.42 ± 0.3	0.64 ± 0.2	1.97 ± 0.5
Nearest neighbour distance [µm]	1.75 ± 0.5	0.64 ± 0.2	0.66 ± 0.3

Table 1: Local silanol distribution on differently treated thermal SiO_2.

1.3.2 Probe diffusion in ultrathin TEHOS films

The varying distribution of surface silanols is not only identified in the above described (decoration) experiments, but has also an influence on probe molecule diffusion in ultrathin liquid films. Figure 3 (bottom, experimental data) shows $C(D)_\tau$ obtained for diffusing RhB in ultrathin TEHOS films on thermal oxide for various substrate treatments. Immobile molecules have been omitted according to the position accuracy depending on the particular signal to noise ratio.

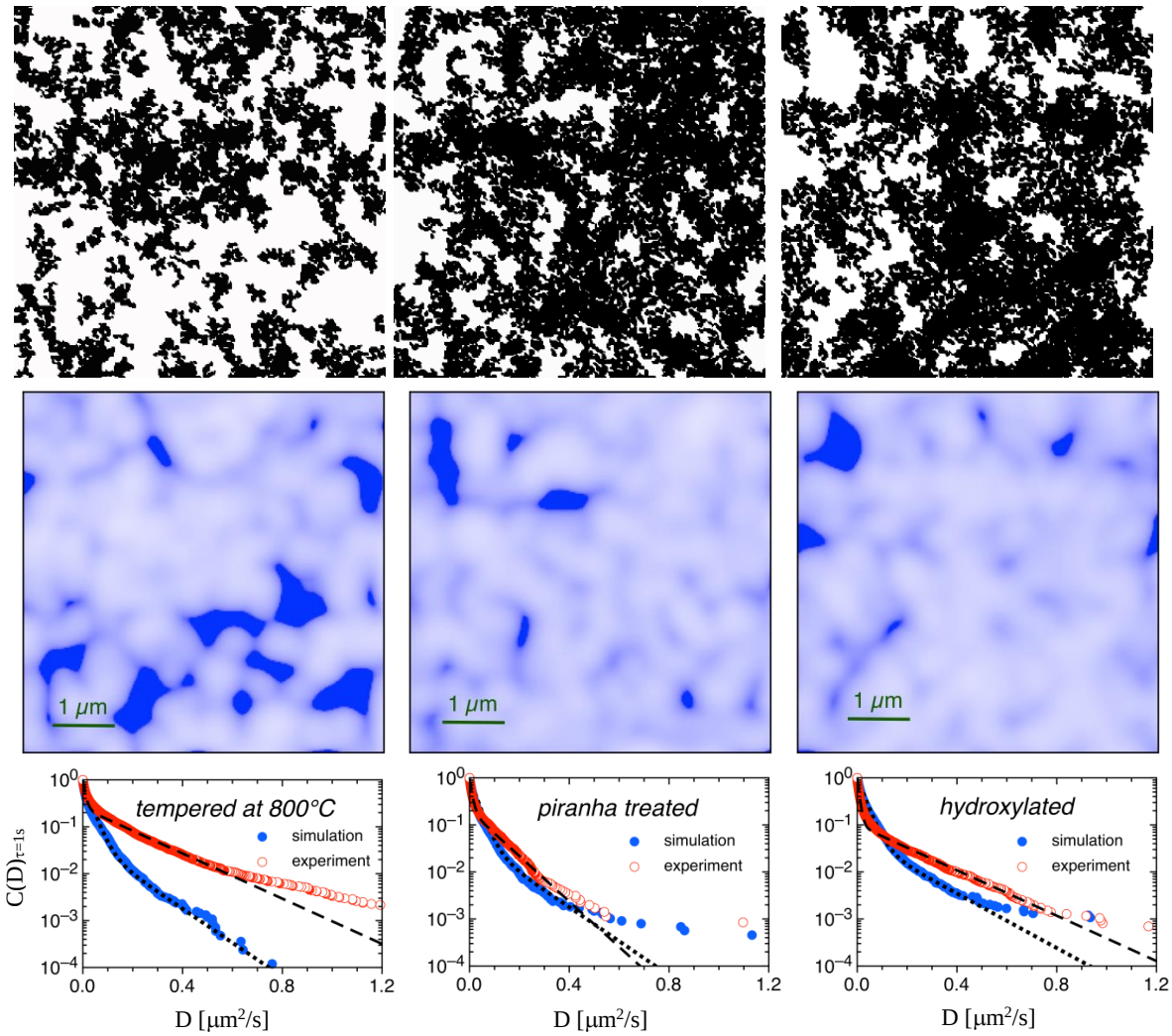

Figure 3: (bottom) Cumulative probability distributions of diffusivities $C(D)_\tau$ from simulations (●) and experiment (○) together with fits according to (2), for simulations (dotted line) and experiment (dashed line) obtained for different experimentally determined silanol distributions such as shown in Figure 2: (left) tempered, (middle) piranha treated and (right) hydroxylated substrates. (top) heterogeneous substrate coverage used for the simulation, areas with slow diffusion are black. (middle) time integrated fluorescence intensities obtained from tracking analysis with tracking.sh.

As can be seen, the $C(D)_\tau$ (Figure 3 bottom) deviate from a mono-exponential behavior for all three kinds of substrate treatments. The analysis of heterogeneous diffusion is not straightforward and the diffusion coefficients may be derived from fitting experimental data only in some particular cases using only two distinct components [15, 22, 26]. Nevertheless, an approximation using a sum of two exponentials, Eq. (2), provides further insights into probe diffusion behavior.

$$C(D)_\tau = A_1 \exp(-D/D_1) + A_2 \exp(-D/D_2), \quad \text{with} \quad A_1 + A_2 = 1. \tag{2}$$

This simplified approach has been used since we suggest a simple 2-layer model as described in Figures 4 and 5. Naturally, more complex fitting functions would fit the data more closely. The results from fitting the data with (2) are given in Table 2. In case of the piranha treated substrate, the bi-exponential approximation fits the experimental data quite well, whereas for the hydroxylated substrates larger diffusivities are observed. These deviations are even more pronounced in case of the tempered substrate. However, deviations only occur in the amplitude range of 10^{-2} to 10^{-3}. Moreover, only a few

data points can be collected for fast diffusion in case of high silanol coverage (middle and right graph). The amplitudes A_1 for the slow component increase from the “tempered” to the “hydroxylated” substrate thereby following the increase of coverage with surface silanols as given in Table 1.

These findings can be interpreted using a simple lateral two-region model as depicted in Figure 4. We assume that probe molecules diffuse on top of the silanol clusters with an effective diffusion coefficient D_{slow}, whereas they diffuse with D_{fast} between the clusters. The slow diffusion on the silanol clusters is caused by adsorption/desorption kinetics during the image exposure time. In case of probe molecules with two possible H-bonding sites (as it is the case for RhB), also some kind of surface gliding by successive building and breaking of H-bonds with neighboring surface silanols may be considered, as suggested by Honciuc et al. [27]. The here described experiment did not allow for discrimination between fast re-adsorbtion dynamics and surface gliding. The slow effective diffusion will depend on the particular probe molecule chemistry.

D_{fast} cannot be directly derived from the silanol density distribution. The diffusion coefficient of RhB in bulk TEHOS is about 50 µm²/s [15]. Thus, the probe molecule would diffuse across an effective area of about 50 µm² during an exposure time of 1 s which is considerably larger than the average area separating neighboring silanol clusters (see Figure 2). Therefore probe molecules diffuse with D_{fast} only part of the image exposure time. The remaining time they will diffuse with D_{slow} on top of the silanol clusters.

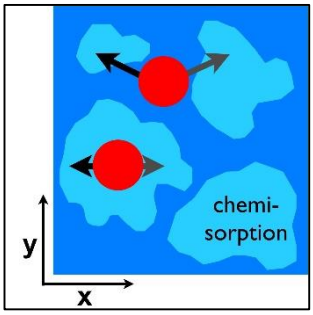

Figure 4. Influence of interface heterogeneity on probe molecule diffusion including physi- or chemisorption [15].

For this reason, the geometry of the silanol clusters and the interspacing region has an essential influence on the probability distribution of diffusivities. On the piranha treated substrate, silanols constitute many small clusters resulting in a narrow cluster size distribution with a small and quite regular interspacing distance. Thus, the correlated diffusivities show an almost mono-exponential dependence for diffusion coefficient D_2. In this case, D_2 resembles the average diffusion coefficient for fast probe molecules. On contrary, in case of the tempered and the hydroxylated substrate, silanol cluster sizes and the interspacing distances show a much broader distribution. Therefore, diffusivities are not mono-exponentially distributed. For the tempered substrate, the much larger interspacing areas lead to a stronger contribution from longer transients, increasing the probability for larger diffusivities.

1.3.3 Simulation of diffusion influenced by surface heterogeneities

To further evaluate the influence of substrate surface heterogeneities on diffusion coefficients, we performed simulations using a vertical two layer model. Within the software package *dsaa*, Heidernätsch had developed a simulation tool which allowed to incorporate structured substrates into a multi-layer model and simulates also wide-field acquisition of probe molecule diffusion [26]. Figure 5 (top) illustrates two-layer diffusion for a model substrate (top, right) containing stripes with reduced mobility (black). In the model (top, left), a reduced diffusion coefficient $D_{1\mathrm{a}}$ is used in layer 1 on the black areas of the substrate, while on the white areas, the diffusion coefficient $D_{1\mathrm{b}}$ was set equal to the top-layer diffusion coefficient D_2. Figure 5 (bottom) shows the results from analyzing simulated wide-field data with the tracking package *tracking.sh* [12, 15]. For this simulation the diffusion coefficients have been set to $D_{2*} = D_{1\mathrm{b}*} = 1$ µm²/s and $D_{1\mathrm{a}*} = 0.01$ µm²/s with exchange rates $f_{12} = 0.5$ s^{-1} and $f_{21} = 0.01$ s^{-1} between the upper and lower layer and a time step $\mathrm{d}t = 0.1$ ms. The wide-field acquisition was simulated with an exposure time $\Delta t = 1$ s for each frame and a total number of 1800 subsequent frames. Figure 5 (bottom right) shows simulated intensities integrated over all 1800 frames on a scale ranging from low (blue) to high (white) fluorescence intensities. The stripes with slow diffusion (black) in layer 1 correspond to high fluorescence intensities, separated by low intensity stripes marking the areas with fast diffusion. The lower intensity between stripes of slow diffusion is related to the fact that for fast diffusing molecules the detected intensity will be smeared out over a wider area during one time step. Additionally, the stationary distribution of probe molecules yields a higher probability for molecules on the stripes with correlated slow diffusion.

Figure 5 (bottom, left) shows the simulation of the cumulated probability distribution of diffusivities from all detected trajectories together with a fit according to (2). On the time scale of the observation, the diffusion is heterogeneous, as can be seen from the fit deviating from a straight line. We obtain effective diffusion coefficients $D_1 = 0.012$ µm²/s and $D_2 = 0.055$ µm²/s with amplitudes $A_1 = 0.9$ and $A_2 = 0.1$, respectively. The obtained effective diffusion coefficients are intermediates between the diffusion coefficients $D_{1\mathrm{a}*} = 0.01$ µm²/s and $D_{2*} = D_{1\mathrm{b}*} = 1$ µm²/s used for the simulation and do not correspond to the real diffusion coefficients. While $D_{\mathrm{slow}} = D_1 = 0.012$ µm²/s gives a reasonable value for diffusion across silanol clusters with short excursion into the upper film region, $\mathrm{D}_{\mathrm{fast}}$ cannot be retrieved from these simulations, whereby $D_2 = 0.055$ µm²/s gives rather an average for very fast and the slow diffusion.

To proceed further towards a more realistic silanol related cluster model, we used the experimentally obtained silanol distributions (see Figure 2) as heterogeneous substrates as a base for the simulations using the same diffusion parameters as for the previously described model simulations. Figure 3 (top) shows the heterogeneous substrates with (left) tempered, (middle) piranha treated, and (right) hydroxylated surface. Again, areas of slow diffusion are shown in black. The related integrated intensities from analysis of the simulated acquisitions using tracking.sh are shown in Figure 3 (middle). Figure 3 (bottom) shows probability distributions $C(D)_\tau$ obtained from the detected trajectories from simulation (●) and in comparison to experimental (○) diffusion of RhB in ultrathin TEHOS films on the differently treated substrates. Fitting data are collected in Table 2.

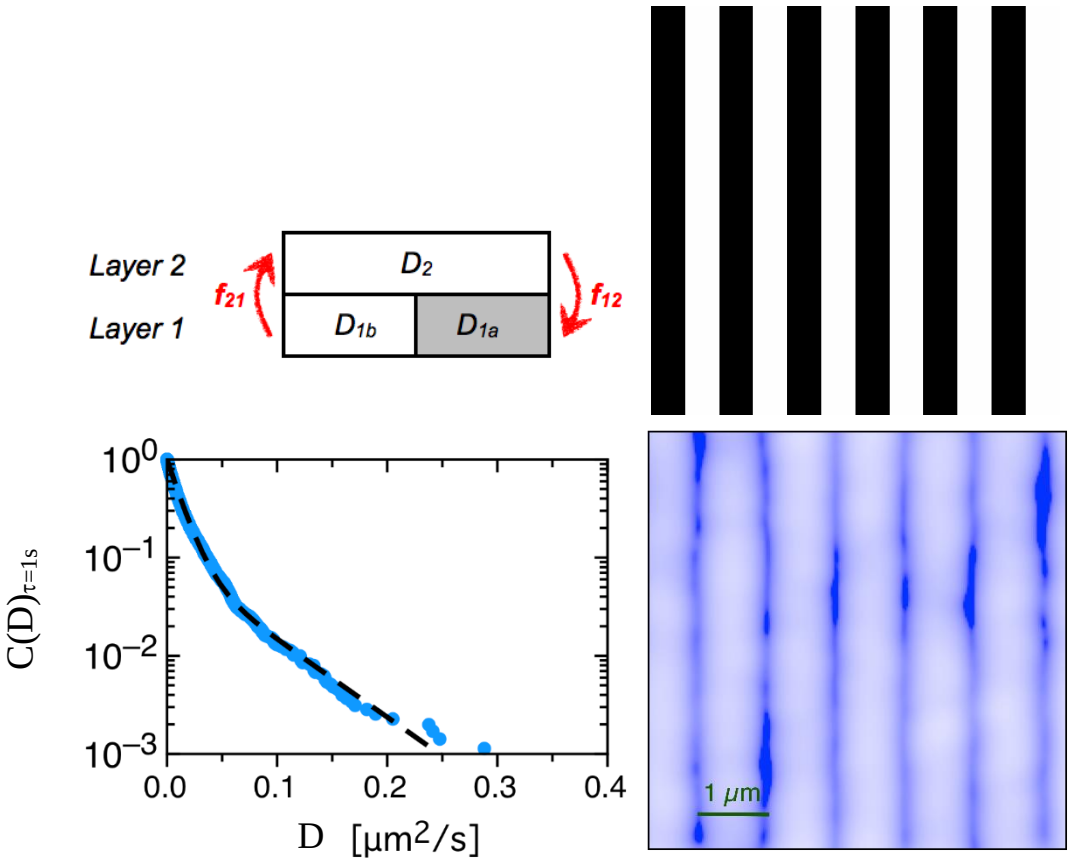

Figure 5: Structured model substrate (top, left) two-layer model with a (top, right) substrate with alternating distributions of D_{1b} (slow) and D_{1a} (fast) diffusion. (bottom, left) Simulated cumulative distribution of diffusivities with a fit (dashed line) according to (2); (bottom, right) accumulated fluorescence intensity.

$C(d_{diff,})_\tau$	A_1	D_1 [µm²/s]	A_2	D_2 [µm²/s]
tempered, experiment	0.61 ± 0.02	0.012 ± 0.002	0.39 ± 0.02	0.13 ± 0.02
tempered, simulation	0.95 ± 0.02	0.028 ± 0.005	0.05 ± 0.02	0.12 ± 0.02
piranha, experiment	0.68 ± 0.02	0.015 ± 0.003	0.32 ± 0.02	0.09 ± 0.01
piranha, simulation	0.95 ± 0.02	0.028 ± 0.005	0.05 ± 0.02	0.12 ± 0.02
hydroxyl., experiment	0.80 ± 0.02	0.010 ± 0.002	0.20 ± 0.02	0.13 ± 0.02
hydroxyl., simulation	0.95 ± 0.02	0.030 ± 0.005	0.05 ± 0.02	0.15 ± 0.02

Table 2: Parameters from bi-exponential fits according to (2) to the experimental and simulated diffusivities $C(D)_\tau$ shown in Figure 3.

The slow diffusion on the silanol clusters appears as areas with high fluorescence intensities (white) in the integrated images (Figure 3 middle). Large areas without clusters appear dark (blue). Fluorescence intensity variations are also found in integrated images from experimentally determined silanol cluster distributions (see Figure 1 left), pointing to an influence from heterogeneous silanol distributions on probe molecule diffusion. A similarity between fluorescence intensity distributions according to probe molecule diffusion (middle) and decorated silanol cluster distribution (top) is clearly observed.

$C(D)_\tau$ obtained from the simulations show tentatively a larger amplitude of the slow component as compared to the experimental ones, see Figure 3 (bottom) and Table 2. In contrast to simulations, the experimental data contain immobile molecules. In general, fitting diffusivity distributions $C(D)_\tau$ yields diffusion coefficients of comparable magnitude both for simulations and experiments for all three

substrate treatments. The best overall agreement between simulation and experiment is obtained for the piranha treated substrate. Here the almost regularly distributed small silanol clusters result in a rather homogeneous substrate surface leading to a more homogeneous lateral diffusion. Consequently, the slow and fast components obtained from fits to experimental data yield the smallest difference with $D_1 = 0.015$ µm²/s and $D_2 = 0.09$ µm²/s (see Table 2). The largest deviation between $C(D)_\tau$ from experiment and simulation is found for the tempered substrate (see Figure 3 bottom left). In this case the simulation can be described nearly bi-exponential. According to Table 1 the nearest neighbor distance is in the tempered case much larger than for the other 2 surfaces. However, the simulation is – if restricting to a simple bi-exponentially approximation – not very sensitive to the kind of substrate. Additionally, the fitted amplitudes of the fast component are with respect to the experiment underestimated, especially for the tempered substrate for which an apparently third still faster component does not show up at all.

The reason for these deviations is probably due to the fact that the simple approximation of only 2 diffusion coefficients and exchange rates, respectively, does not hold. However, in a first step we intended to keep the simulation model as simple as possible. We suggest that the exchange rates between the layers depend on the underlying structure itself and the ratio f_{21}/f_{12} should be increased for the tempered substrate. Moreover, the diffusion in the upper film layer and the silanol-free areas was set to $D_{2*} = 1$ µm²/s for the simulation. However, the bulk diffusion coefficient of RhB in TEHOS is about 50 µm²/s [15], which is much faster than 1 µm²/s set for diffusion in the upper film layer. Keeping in mind that all diffusion parameters (including exchange rates f_{ij}) have been assumed to be the same for all 3 substrates the general trend of the simulations of $C(D)_\tau$ supports the concept of slowed lateral diffusion on surface silanol clusters.

In this study we have used surface silanol distributions on differently treated silicon substrates with thermally grown oxide to show how substrate surface heterogeneities influence probe molecule diffusion in ultrathin liquid films. Increasing the heterogeneity by either increasing the average silanol cluster size or the mean distance between the clusters, enhances the heterogeneity in probe molecule diffusion. Simulations employing an oversimplified two-layer model with a (realistic) heterogeneous substrate structure support the concept of slow and fast lateral diffusion across areas on the substrate containing silanol clusters and silanol-free areas, respectively. However, the simulations have to be extended to allow for structure related variations of the simulation parameters.

Two further studies not discussed here, investigate the influence of heterogeneous substrate structures on diffusion of nanoscale Ag clusters in surface water layers on silicon oxide substrates [28, 29]. Additionally to the superficial heterogeneities, also long-range interactions, as for example van der Waals forces, have an impact on interfacial mobility and probe molecule diffusion [30]. For intrinsically structured materials such as liquid crystals, there is an additional impact of structure related changes at solid-liquid interfaces on probe molecule diffusion [31–33].

2 Comparing transport properties obtained using single particle and ensemble observations

2.1 Introduction

Mass transfer processes occurring in materials with specific interactions may lead to complex diffusion behavior, such as the occurrence of transient sub-diffusion or of heterogeneous diffusion. Diffusion is the irregular, omnipresent motion of the elementary constituents of matter. Historically, diffusion measurements were based on the observations of large ensembles of diffusing particles [34]. The recently emerged single-particle tracking (SPT) or fluorescence correlation spectroscopy (FCS), in which either single molecules or their small ensembles are traced, have provided a totally new view of diffusion [35–37]. At the same time, these developments posed a problem of inter-relating the messages delivered by these two classes of experimental techniques. The latter was in the focus of the present work. The results and their discussions presented here concern several selected systems, in which the traced markers were small molecules [38, 39], polymer globules [40], and crystal-fluid interfaces in channel-like disordered pores [41–43]. These three different systems considered represented three different situations in which the relevant characteristic time scales of the underlying transport processes were (i) notably shorter, (ii) of the order of, and (iii) notably longer than the experimental time scale, respectively. In this way, with the former (i) and the latter situations (iii) we have mimicked ergodic and non-ergodic systems, respectively; for the intermediate case (ii), according to the literature data anomalous diffusion consistent with the fractional Brownian motion or obstructed diffusion was anticipated to occur [44].

To address these problems experimentally, we used two different techniques of NMR, namely pulsed field gradient (PFG) NMR [45] to directly probe the mean square displacements (MSD) and NMR cryoporometry [46] to follow propagation of the solid-liquid interfaces in nanochannels. The thus assessed quantities represented ones averaged over large ensembles. The results obtained were compared to those obtained either using SPT or FCS. Starting with the most simple system exhibiting normal diffusion we experimentally demonstrate the validity of the ergodic theorem for diffusion. For more complex systems, we report on the discrepancies existing between the two methods and discuss the underlying reasons.

2.2 Results and discussion

2.2.1 Experimental confirmation of the ergodic theorem

As a trivial, but as a necessary and experimentally challenging step, before any studies in which time- and ensemble-averaged transport quantities are correlated, one shall be concerned with the experimental demonstration of the validity of the ergodic theorem for systems, in which it is expected to be valid. In these systems, all microscopic time scales should be notably shorter than the experimental one. Despite being generally accepted, the proof of the equivalency of the ensemble- and time-averaged MSD,

$$\langle r^2(t)\rangle_{\mathrm{ensemble}} = \langle r^2(t)\rangle_{\mathrm{time}}, \tag{3}$$

remained not addressed experimentally. Mainly, this was caused by the mutually contradicting measuring conditions inherent in the two experimental approaches, in particular in NMR and in SPT. In SPT, the trajectories of the diffusing single molecules are constructed by fitting the positions of the molecules over time [35]. Therefore the fluorescence signals of the molecules have to be clearly separated from each other, demanding their very low concentrations. Additionally the measurements are limited by the signal-to-noise ratio, which is determined by the brightness of the dye molecules and the integration time. Hence, there is an upper limit for the detectable diffusivity in SPT. Exactly the opposite conditions, namely high concentrations (for generating sufficiently strong NMR signal requiring at least 10^{18} nuclear spins in the samples) and high diffusivities (for giving rise to observable displacements) must be fulfilled for PFG NMR [45].

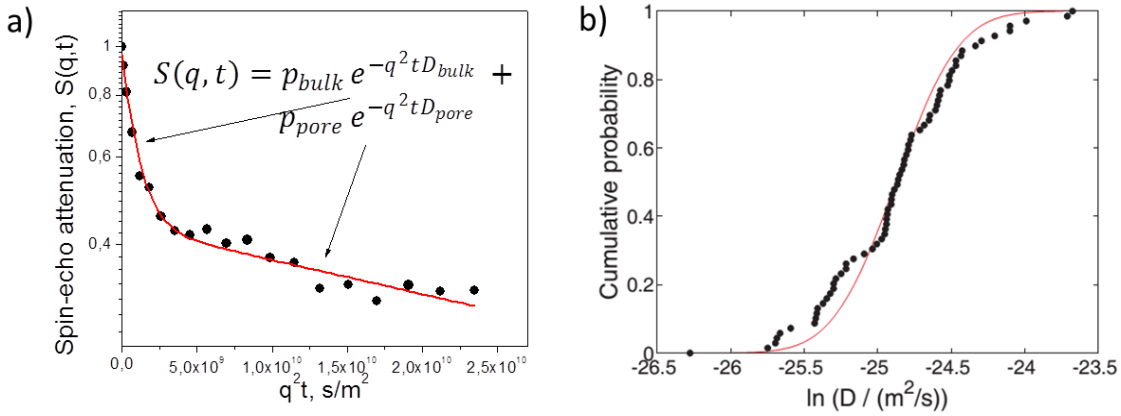

Figure 6: (a) Normalized spin-echo diffusion attenuations measured for Atto532 dissolved in deuterated methanol in nanoporous glass using PFG NMR. The two slopes correspond to the Atto532 diffusivities in the nanopores and in the excess bulk phase. (b) Cumulative distributions of the diffusivities measured using SPT (from Ref. [38]).

In order to match the measurements conditions for PFG NMR and SPT studies, we have applied nanoporous glass as a host system for the solution of Atto532 dye molecules in an organic solvent as a guest ensemble. The diffusivity of Atto532 in a nanoporous glass depends on their concentration. For high concentrations it is governed by guest-guest and host-guest interactions, whereas for low concentrations the latter mechanism dominates. While single-molecule experiments were performed in the low-concentration regime ($\sim 10^{-11}$ mol/l), we managed to reduce the concentration in the PFG NMR experiments to approach this concentration regime corresponding to about 10^{18} protons of Atto532 in the sample contributing to the NMR signal. Further on, by purposeful tuning the pore diameter of the nanoporous glass down to 3 nm, the diffusivity of Atto532 was adjusted to a range of the values accessible by both techniques. As an example, Figures 6a and 6b show the NMR signal diffusion attenuation and the cumulative diffusivity distribution (defined in Section 3.1) measured for identical samples and under identical conditions using PFG NMR and SPT, respectively. They yield within the experimental accuracy the equal average diffusivities of Atto532 in the nanopores of $(1.2 \pm 0.5) \cdot 10^{-11}$ m^2/s.

For the first time, single-molecule and ensemble diffusion measurements were found to experimentally confirm the hypothesis of ergodicity for a simple system exhibiting normal diffusion. With this important step being made, the experimental approach developed can be extended to more

complex systems, including those for which Eq. (3) may not hold. Our current activities concern, in particular, with systems exhibiting normal diffusion but having broad distributions of diffusivities of the diffusing species. This can be observed, e.g., in diluted polymer solutions with high polydispersity indices. Intrinsic peculiarities inherent in the two experimental methods render the distributions of the measured diffusivities to deviate from each other. Elucidating the particular mechanisms for this observation is currently under progress.

2.2.2 Systems displaying anomalous diffusion

With the experiments described in the preceding section, the two so-far separated worlds of diffusion measurements have been brought together for a situation where the rules of normal diffusion are obeyed. However, single particle observations of, e.g., biological systems [47, 48] often seem to exhibit patterns of anomalous diffusion in which

$$\langle r^2(t)\rangle \propto t^{\alpha}, \tag{4}$$

where $\alpha < 1$. It is further anticipated that weak-ergodicity breaking may also accompany these processes. Most importantly, Eq. (4) has been found to hold also in artificial polymeric mixtures, mimicking overcrowded environments in bio-systems. In particular, anomalous diffusion of different tracer molecules in aqueous solutions of high-molecular-mass dextran acting as a crowding agent as studied using fluorescence correlation spectroscopy (FCS) operating with very small molecular ensembles has been reported [49, 50]. The dependencies of the anomaly exponent on different parameters, such as molecular mass of probe and matrix molecules have been reported. This allows for comparative studies of similarly prepared model samples using different techniques, which may shed further light into microscopic mechanisms leading to anomalous diffusion.

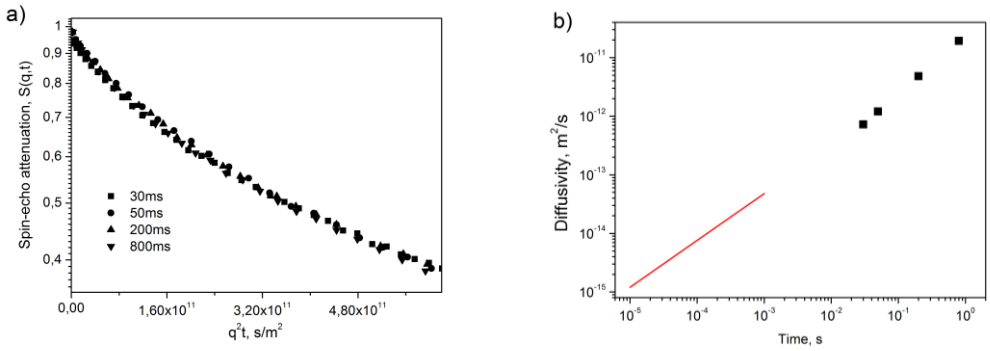

Figure 7: (a) Spin-echo diffusion attenuations measured using PFG NMR for aqueous solution of dextran mixture. Different symbols refer to different diffusion times shown in the inset. (b) Mean square displacements as a function of diffusion time t obtained from the data of Figure 2a. The solid line is a function $Kt^{0.8}$ showing the slope resulting from FCS studies of a similar system.

Among different model systems exhibiting anomalous diffusion reported in Refs. [49, 50], we have chosen a mixture of 40 kDa and 500 kDa dextranes dissolved in deuterated water (the water mass fraction of about 20 %). This choice was dictated by the fact that this particular system yielded the most optimal conditions for the diffusion measurements using PFG NMR in a broad range of the diffusion times from 30 ms to 800 ms. This primarily concerned (i) the diffusivities accessible by this technique

(above 10^{-14} m^2/s) and (ii) the sufficiently long nuclear magnetic relaxation times allowing the PFG NMR experiments to be performed, but still keeping the anomaly exponent notably below 1. Thus, for the particular system studied it was expected to be about 0.8.

In systems with normal diffusion the NMR spin-echo signal diffusion attenuation has the simple form

$$S(q,t) \propto \exp(-q^2 t D_0), \tag{5}$$

where q is the wave number and t is the diffusion time. The measured diffusion attenuations S, which are shown in Figure 7a, exhibited no dependency on the diffusion time t, i.e. collapsed into one master curve by plotting $\ln(S)$ versus $q^2 t$. Note that this way of plotting corresponds to a rescaling of the squared displacements by the time lag, as it is done in the definition of the distribution of diffusivities (Section 3). This fact reveals that the diffusivities are constant over intervals of the diffusion times t from 30 ms to 800 ms. In turn, this means that the MSD grows linearly with time as shown in Figure 7b. For comparison, the solid line in Figure 7b also shows the prediction for a similar system obtained using FCS which covers, however, notably shorter diffusion times. The gap existing between the diffusion data obtained using two techniques does not allow making definitive conclusions whether the discrepancy is due to a transient behavior at short time scales or whether there is a fundamental issue resulting in the discrepancy.

2.2.3 Propagation of solid-liquid interfaces in disordered nanopores

The third class of the systems studies concerned those in which the time scales of the microscopic processes notably exceeded the laboratory time scale. Such situations can experimentally be realized and studied by following phase transitions occurring in nanoporous materials. Because these transitions are intrinsically activated processes, i.e. they require overcoming of the barriers in the free energy, and exploiting the fact that, under the conditions of spatial confinements in nanoporous solids, these energy-barriers becomes pore-size-dependent, mesoscopic disorder of the pore structure may give rise to a broad distribution of the barrier heights. Consequently, this disorder is translated into the respective disorder in the spatial phase transition rates [51, 52]. Under suitable conditions, translational dynamics of the interface between the two phases can be probed.

As nanoporous material, we used silicon wafers in which macroscopically long channels possessing mesoscopic variation of the channel diameter were etched electrochemically [53]. In our work we have studied kinetics of the freezing transition of the fluids confined to the thus obtained nanochannels. By choosing a suitable liquid, for which homogeneous nucleation of the crystals phase was strongly suppressed, transition was forced to occur solely via invasion of the crystalline phase from the pore openings, where the seed of the crystal were provided. By carefully tuning the experimental temperature, which determines the gradient in the chemical potential between the intra-pore and outer-pore fluids, the freezing transition was adjusted to occur by extremely slow propagation of the invading crystal front or of the fluid-crystal interface.

The typical MSD of the ice freezing fronts' positions propagating into nanochannels measured using NMR cryoporometry [41, 54], is shown in Figure 8a. Notably, the results obtained represent an average over more than 10^6 channels with different statistical disorder realizations. It is important to note that the

results obtained reveal the occurrence of aging, i.e. the kinetics measured immediately after the temperature quench depended on how long the system was kept (aged) at a higher temperature. Our intention was to access the interface dynamics on a single channel level, which however had turned to be a difficult experimental task. We have therefore followed an alternative route by developing a microscopic (theoretical) model being capable to capture the most important experimental observations reported in the literature concerning freezing and melting transitions in confined spaces without any *a priori* assumptions inherent to theoretical models developed so far. The model developed [43] for the freezing and melting transitions occurring in pore spaces with arbitrary pore geometries was based on the Kossel-Stranski crystal-growth model [55]. It is reminiscent of the random field Ising model and can most efficiently be analyzed using Dynamic Monte Carlo (GCMC) simulations. Dynamics of other transitions, e.g. of liquid-gas, can as well be analyzed [56].

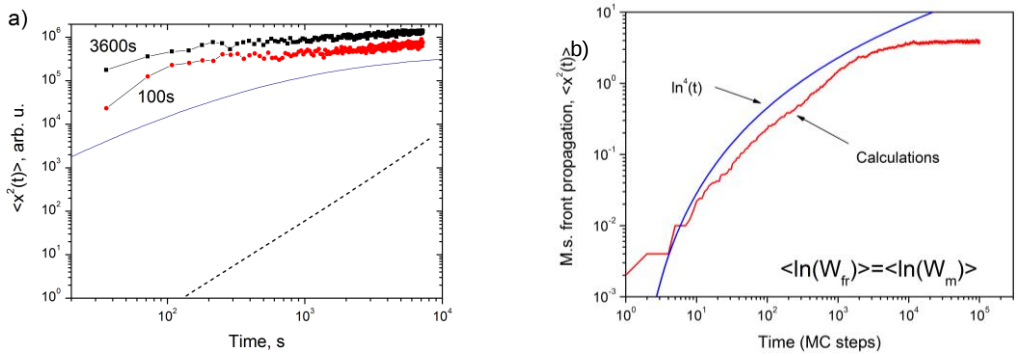

Figure 8: (a) Propagation of the freezing front for water into mesoporous silicon with 5 nm average pore diameter after the temperature quench to −35 °C from −34 °C. At −34 °C the system was kept 100 s (circles) and 3600 s (squares). The solid and broken lines show the ensemble- and moving time averaged MSD obtained in computer simulations, respectively. (b) Average mean square ice-front position in disordered channels at the pore equilibrium temperature exhibiting Sinai diffusion behavior.

In addition to the experimentally measured freezing kinetics Figure 8a shows the ensemble-averaged MSD for the interface positions obtained using the model developed. They were calculated using Dynamic Monte Carlo simulations modelling the transition kinetics in the channel-like pores with disorder and are found to reproduce qualitatively the experimental ones. In addition to the ensemble-averaged $\langle x^2(t)\rangle_{\mathrm{ensemble}}$ also the similar quantity $\langle x^2(t)\rangle_{\mathrm{time}}$ obtained using moving time average of the transition progress in a single channel is shown. The notable discrepancy between $\langle x^2(t)\rangle_{\mathrm{ensemble}}$ and $\langle x^2(t)\rangle_{\mathrm{time}}$ signals formally about the ergodicity breaking. This becomes especially clear when the quench temperature is chosen to remove the bias in the chemical potential. In this case, as demonstrated by Figure 8b, the Sinai diffusion regime emerges. For this regime the occurrence of the weak-ergodicity breaking is known [57].

In this work we have addressed correlation between the diffusion data obtained using two different experimental approaches based on single molecule and ensemble observations. By first selecting a system exhibiting normal diffusive behavior, we experimentally prove the ergodic theorem for diffusion by directly comparing the results obtained for the mean square displacements measured using NMR (ensemble average over about 10^{18} molecules) and single particle tracking (moving time average of a single molecule trajectory) [38]. As the next step, we considered diffusion of large, several nanometer big polymer globules diffusing in a medium containing larger polymer species [40]. The latter, which

mimics crowded environments in biological cells, has been shown to give rise to anomalous sub-diffusion as observed using fluorescence correlation spectroscopy. Our studies performed using pulsed field gradient NMR revealed no anomaly, but on larger time scales. As a challenging future task, eliminating the still existing lag between the two techniques may provide further insight into microscopic dynamics. Finally, using NMR cryoporometry method we addressed spatial propagation of solid-liquid interfaces in disordered nanoporous channels [43, 52]. It was found that this dynamics is reminiscent of translational dynamics with disordered transition rates. A microscopic model of the phenomenon has been developed. The transition dynamics assessed using this model has proven that propagation of the solid-liquid interfaces in disordered pores exhibits non-ergodic behavior consistent with aging observed in the experiments.

3 Analyzing heterogeneous, anisotropic, and anomalous diffusion processes by the distribution of diffusivities

3.1 Introduction

Experimental or numerical data from diffusion processes are typically evaluated in terms of the mean-squared displacement (MSD). However, for heterogeneous and anisotropic systems, which are characterized by more than one diffusion coefficient, as well as for anomalous diffusion, where different physical mechanism can lead to the same temporal behavior of the MSD, a more advanced analysis is needed. For this purpose, the distribution of diffusivities is well suited. We give an overview of its basic properties and discuss its benefits.

Investigations of heterogeneous diffusion processes, where the diffusion coefficient changes with time revealed that well-established methods such as mean-squared displacement (MSD) analysis conceal the effects of inhomogeneous processes [58]. Hence, a new analysis tool has been suggested which was applied successfully to heterogeneous processes observed with SPT [22]. Furthermore, its relation to the signal attenuation of ensemble-based techniques such as pulsed-field gradient nuclear magnetic resonance was shown [22].

The displacements of diffusive motion are a fluctuating quantity along a trajectory. However, due to averaging for the MSDs only a mean value is analyzed and the characteristic fluctuations are lost. In order to avoid this disadvantage, we introduced the distribution of diffusivities as a powerful tool for analyzing trajectories of complex diffusion processes [58]. It considers the fluctuating diffusivities along a trajectory, which are displacements rescaled by their corresponding time lag, in an intuitive way.

The definition of the distribution of diffusivities is briefly recalled as

$$p(D,\tau) = \langle \delta[D - D_t(\tau)] \rangle, \tag{6}$$

where $\langle \dots \rangle$ either denotes an ensemble average or a time average $\langle \dots \rangle = \lim_{T\to\infty} 1/T \int_0^T \cdots \mathrm{d}t$, which is typically applied for SPT experiments. The diffusivities $D_t(\tau)$ are calculated from the displacements $\mathbf{r}_t(\tau) = \mathbf{x}(t+\tau) - \mathbf{x}(t)$ during a given time lag τ between two snapshots of the d-dimensional trajectory

by

$$D_t(\tau) = \frac{[\mathbf{x}(t+\tau) - \mathbf{x}(t)]^2}{2d\,\tau}. \tag{7}$$

These definitions can easily be applied to experimental data from trajectories obtained from the video microscope. The corresponding displacements are transformed to diffusivities, which are binned into a normalized histogram to estimate their probability density function. Note that for statistical reasons the cumulative distributions of diffusivities were considered in the experimental sections, Sections 2 and 3, which are just integrals of the density defined in Eq. (6). I.e. $\mathrm{C(D)}_\tau$ used in Eqs. (1) and (2), is given by $\mathrm{C(D)}_\tau = \int_D^\infty p(D',\tau)\,dD'$, and the distribution used in Section 1.3.3 is given by $1 - \mathrm{C(D)}_\tau$. Differentiating these cumulative distributions gives the density treated here.

Important quantities are the moments $M_m(\tau)$ of order m

$$M_m(\tau) = \langle D_t(\tau)^m \rangle = \int_0^\infty \mathrm{d}D\; D^m\, p(D,\tau). \tag{8}$$

Their τ-dependence can reveal characteristic properties of the underlying process such as time scales on which the diffusion coefficient changes. In the limit $\tau \to \infty$ for normal diffusion the first moment coincides with the mean diffusion coefficient $\langle D \rangle$ which determines the slope of the MSD $\langle \mathbf{r}(\tau)^2 \rangle \propto 2d\,\langle D \rangle\,\tau$ [17].

For d-dimensional isotropic homogeneous diffusion processes, which are governed by one single diffusion coefficient D_c, the distribution of diffusivities yields

$$p(D,\tau) = p_{D_c}(D) = \left(\frac{d}{2D_c}\right)^{d/2} \frac{D^{d/2-1}}{\Gamma(d/2)} \exp\left(-\frac{d}{2\,D_c} D\right), \tag{9}$$

where $\Gamma(\mathrm{x})$ denotes the gamma function. Equation (9) directly results from the sum of the squares of d independent and identically distributed Gaussian random variables with zero mean and variance D_c/d. Hence, it is known as the χ^2-distribution of d degrees of freedom.

Based on these definitions and elementary results more complex processes such as anisotropic diffusion, processes with extended state space, heterogeneous, or anomalous diffusion can be investigated.

3.2 Results and discussion

3.2.1 Anisotropic processes

Anisotropic diffusion processes have been found in many applications comprising transport in anisotropic media [21, 31, 59]. Instead of a characterization by one single diffusion coefficient, the transport properties depend on the direction of the motion. Hence, advanced data analysis has to be applied to determine the characteristic quantities of the process which are concealed by methods such as MSD. Quite formally these processes are described by a propagator involving a diffusion tensor $\widehat{\mathbf{D}}$ with eigenvalues corresponding to the diffusion coefficients $D_1, D_2, \ldots, D_d$ along the principal axes of the d-dimensional system [60]. This propagator can be transformed to the distribution of diffusivities [67].

The asymptotic behavior of the distribution of diffusivities can be exploited to identify the anisotropy of homogeneous diffusion processes. An asymptotic expansion for large D yields the leading behavior of the distribution of diffusivities in the logarithmic representation given by

$$\log p_{\hat{\mathbf{D}}}(D) \overset{D\to\infty}{\sim} -\frac{d}{2\,D_\infty} D, \tag{10}$$

where $D_\infty = \max(D_1, D_2, \ldots, D_d)$. Hence, Eq. (10) denotes an exponential decay proportional to the largest diffusion coefficient which contributes to the anisotropic system.

For homogeneous isotropic systems the exponential decay in Eq. (10) is governed by the isotropic diffusion coefficient $D_\infty = D_c$. The first moment $\langle D \rangle$ of the distribution of diffusivities coincides with D_c whereas for anisotropic systems $\langle D \rangle < D_\infty$. Due to this difference the distribution of diffusivities deviates from the χ^2-distribution given by Eq. (9). Hence, it is natural to define the quantitative measure

$$\eta = \frac{D_\infty}{\langle D \rangle} - 1 \tag{11}$$

for characterizing the deviation from the isotropic homogeneous case. A discrepancy between $\langle D \rangle$ and D_∞ detects the existence of several distinct diffusion coefficients contributing to the process. Given the assumption of a homogeneous process, heterogeneities are ruled out such that the discrepancy can only be caused by an anisotropy in the system. Hence, η quantifies the anisotropy of the homogeneous process. For isotropic systems $\langle D \rangle$ and D_∞ coincide and result in a vanishing η. In contrast, the largest possible anisotropy of a d-dimensional system will be reached if one diffusion coefficient, denoted by D_∞ as defined in Eq. (10), is much larger than the others. This yields $\eta = d - 1$ since the first moment is dominated by D_∞ and $\langle D \rangle \to D_\infty / d$. It should be noted that the maximum of η depends on the dimensionality d of the system.

The advantage of the measure of anisotropy as defined in Eq. (11) is obvious since it is easy to obtain the two necessary quantities from experimental data. By averaging the observed diffusivities the first moment of the distribution of diffusivities is determined, which corresponds to the mean diffusion coefficient $\langle D \rangle$. The largest diffusion coefficient of the system is obtained from a fit to $f(D) = c\ \exp(-\lambda_{\text{fit}}\, D)$ to determine $D_\infty = d/(2\,\lambda_{\text{fit}})$. The effective dimensionality d_{eff} of processes observed in $d \geq d_{\text{eff}}$ dimensions is estimated by $d_{\text{eff}} = 2\,\langle D \rangle\,\lambda_{\text{fit}}$ resulting in $\eta = d/d_{\text{eff}} - 1$. Hence, a process observed in d dimensions will yield the largest $\eta = d - 1$ if the motion is effectively one-dimensional.

Since in general the distribution of diffusivities cannot be calculated analytically, some explicit examples are given. For instance, for two-dimensional anisotropic diffusion it is given by

$$p_{\hat{\mathbf{D}}}(D) = \frac{\exp\left[-\frac{1}{2}\left(\frac{1}{D_1} + \frac{1}{D_2}\right) D\right]}{\sqrt{D_1 D_2}} I_0\left[\frac{1}{2}\left(\frac{1}{D_1} - \frac{1}{D_2}\right) D\right], \tag{12}$$

where $I_0(x)$ denotes the modified Bessel function of the first kind. The moments of the distribution of diffusivities can be calculated analytically as functions of D_1 and D_2. In contrast, the evaluation of experimental data aims at obtaining the diffusion tensor from the distribution of diffusivities. By solving their simultaneous equations, the diffusion coefficients corresponding to the main directions of the

anisotropic system are related to the moments by $D_{1,2} = M_1 \pm \sqrt{M_2 - 2M_1^2}$. The measure to characterize the anisotropy of the two-dimensional anisotropic process is directly related to the moments by

$$\eta = \frac{|D_1 - D_2|}{D_1 + D_2} = \frac{\sqrt{M_2 - 2M_1^2}}{M_1} \tag{13}$$

which again vanishes for isotropic processes.

For three-dimensional processes a limiting case is given by a diffusion tensor $\breve{\mathbf{D}}$ where two eigenvalues coincide. This corresponds to systems where the mobility of a particle in one direction differs from the other two. Hence, such an anisotropy can be induced by the shape of the diffusing particle and is typical for uniaxial molecules. The distribution of diffusivities for three-dimensional homogeneous anisotropic diffusion is reduced to

$$p_{\breve{\mathbf{D}}}(D) = \frac{3}{2} \frac{\exp\left(-\frac{3D}{2D^{\mathrm{II}}}\right) \operatorname{erf}\left(\sqrt{\frac{3}{2}\left(\frac{1}{D^{\mathrm{I}}} - \frac{1}{D^{\mathrm{II}}}\right) D}\right)}{\sqrt{(D^{\mathrm{II}} - D^{\mathrm{I}}) D^{\mathrm{II}}}} \tag{14}$$

with the eigenvalues of $\breve{\mathbf{D}}$ denoted by D^{I} and the two-fold degenerate one by D^{II}. Hence, the particle is disc-shaped for $D^{\mathrm{I}} < D^{\mathrm{II}}$ in contrast to a rod-like shape with $D^{\mathrm{I}} > D^{\mathrm{II}}$ which is typical for elongated molecules. The difference between these cases is depicted in Figure 9.

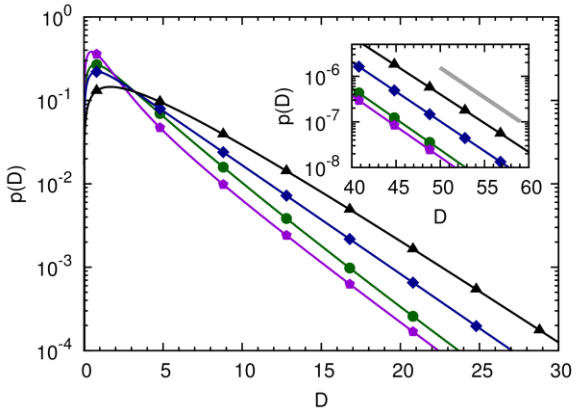

Figure 9: Distributions of diffusivities of homogeneous anisotropic diffusion processes in three dimensions. For uniaxial molecules the distribution is given by Eq. (14), where the curvature after the peak changes from concave for disc-shaped molecules (blue squares; $D^{\mathrm{I}} = 1, D^{\mathrm{II}} = 5$) to convex in the rod-like shapes (violet pentagons; $D^{\mathrm{I}} = 5, D^{\mathrm{II}} = 1$). A further general anisotropic process (green circles; $D_1 = 5, D_2 = 3, D_3 = 1$) obviously shows a qualitative deviation from the isotropic process with the same asymptotic decay (black triangles; $D_c = 5$) which is always concave. The inset depicts the identical asymptotic decays of all processes.

The moments M_1 and M_2 of Eq. (14) are obtained from Eq. (8). These equations can be solved to obtain the eigenvalues of $\breve{\mathbf{D}}$ by $D^{\mathrm{I}} = M_1 \mp \sqrt{3M_2 - 5M_1^2}$ and $D^{\mathrm{II}} = M_1 \pm \frac{1}{2}\sqrt{3M_2 - 5M_1^2}$, where the sign has to be chosen to satisfy the constraint of positive diffusion coefficients. For $\frac{5}{3}M_1^2 < M_2 < 2M_1^2$ both variants of the signs result in positive diffusion coefficients. Then the third moment M_3 has to be calculated from each pair of D^{I} and D^{II} and coincides with the values determined from the data if the correct pair is chosen. Hence, different diffusion coefficients can yield distributions of diffusivities with

identical first and second moments respectively. For vanishing anisotropy, $M_2 \to \frac{5}{3}M_1^2$ and D^{I} and D^{II} approach each other. Hence the single isotropic diffusion coefficient is directly given by the first moment. Close to that limit a decision of the correct pair by M_3 cannot be obtained since both values do not differ significantly.

3.2.2 Processes with extended state space

Evaluating many particles simultaneously can be interpreted as the analysis of a process in an extended state space. As an example, current research addresses the tracking of the motion of elongated molecules, such as deoxyribonucleic acid (DNA), which is labeled with fluorescent dyes at both ends [62]. By combining the positions of both dyes into one state vector a process with extended state space is observed effectively. In this example the contributing positions are highly correlated and do not diffuse independently. The resulting process from simultaneous observation comprises d-dimensional trajectories of N particles. The corresponding state vector $\mathbf{x}(t)$ of the extended state space with effective dimensionality $d_{\mathrm{eff}} = Nd$ of such a process can be interpreted as an d_{eff}-dimensional trajectory. It should be noted that the considerations are independent of the actual structure of the extended state space, i.e., even processes of different dimensionality can contribute. The diffusivities of such processes are determined according to Eq. (7) where the dimensionality d is substituted by the effective one, d_{eff}.

In the simplest case, many particles diffuse simultaneously and independently. Trajectories in the extended state space of non-interacting particles are closely related to anisotropic processes. In general, each of the N independent trajectories is characterized by a different diffusion coefficient, because they may belong to different species. This leads to different diffusive properties in the various directions of the state space. Hence, the distribution of diffusivities can be obtained analogously to anisotropic processes [61], *e.g.*, from the convolution of the contributing processes by $p(D,\tau) = \{p_1 * \cdots * p_N\}(D,\tau)$. As an example, consider the simultaneous tracking of two non-interacting two-dimensional isotropic processes with different diffusion constants D_1 and D_2, respectively, which may stem from the particles diffusing in regions with distinct transport properties, or, from different conformations of a molecule. Such a process is characterized by a diffusion tensor with two two-fold degenerate eigenvalues given by D_1 and D_2. The convolution of the two contributing distributions of diffusivities, which are given by Eq. (9) with $d = 2$ and $D_c = D_1/2$ or $D_c = D_2/2$, respectively, yields

$$p(D) = 2\,\frac{\exp\left(-\frac{2D}{D_1}\right) - \exp\left(-\frac{2D}{D_2}\right)}{D_1 - D_2}. \tag{15}$$

Since the asymptotic exponential decay defined in Eq. (10), is determined by the larger diffusion coefficient, $D_\infty = \max(D_1, D_2) > \langle D\rangle = (D_1 + D_2)/2$ holds. Hence, the anisotropy measure Eq. (11) does not vanish and clearly indicates an anisotropic process. Of course, in the limit $D_1 \to D_2$ the 4-dimensional isotropic process with the distribution of diffusivities given by the χ_4^2-distribution of Eq. (9) is recovered.

3.2.3 Heterogeneous processes

The examples we have presented so far, resulted in a distribution of diffusivities $p(D,\tau)$, which turned out to be independent of τ, *i.e.* $p(D,\tau) = p(D)$. This is a consequence of the homogeneity and the presence of only one simple scaling law in the previous examples. But for instance, in the example of diffusion of a pair of particles, it is easy to show that the presence of e.g. harmonic interactions already leads to a non-trivial τ-dependence of $p(D,\tau)$, which vanishes only in the limit $\tau \to \infty$. An analytically solvable example of such a non-trivial τ-dependence of $p(D,\tau)$ was worked out for a two layer (region) model in [22]. In this example, which is popular in the NMR and SPT community, one could see that $p(D,\tau)$ changes from a bi-exponential form for small τ to a mono-exponential form for $\tau \to \infty$. In the intermediate τ-regime fitting multi-exponential behavior is bound to be inaccurate. This example is a simplification of the heterogeneous model introduced in the first experimental part of this contribution, where also a non-trivial τ-dependence of $p(D,\tau)$ is present. The latter provides the information necessary for distinguishing the models leading to the same behavior in the mean square displacement. As an example we mention the form for the van Hove self-diffusion function proposed for heterogeneous systems in [63], which consists of a weighted superposition of Gaussian propagators. In terms of our distribution of diffusivities, Eq. (6), this would result in a superposition of infinitely many, basically exponential contributions of the form given in Eq. (9). With such a superposition almost arbitrarily decaying distributions can be described. Note, however, that the resulting distribution of diffusivities would be again independent of the time lag, $p(D,\tau) = p(D)$, which neglects that the different diffusive properties typically dominate also on different time scales. An example for the latter for the case of anomalous diffusion is provided below.

3.2.4 Anomalous diffusion processes

Diffusion processes in nature often deviate from the mathematical laws of normal diffusion and behave anomalously, a fact which is often reflected in an asymptotically non-linear increase of the mean-squared displacement $\langle \boldsymbol{r}^2(\tau) \rangle \sim D_\alpha \tau^\alpha$. In the literature, many theoretical models of anomalous diffusion which can lead to the same diffusion exponent α are known [64]. Therefore, the mean-squared displacement is not suitable to discriminate between these models. In this context, an analysis by the distribution of diffusivities provides a significant advantage. To incorporate the non-linear increase of the MSD, the definition of the diffusivities needs to be modified,

$$D_t^\beta(\tau) = \frac{[\boldsymbol{x}(t+\tau) - \boldsymbol{x}(t)]^2}{\tau^\beta} \tag{16}$$

and we now call them generalized diffusivities. The distribution of generalized diffusivities is defined as

$$p_\beta(D,\tau) = \left\langle \delta\left[D - D_t^\beta(\tau)\right] \right\rangle, \tag{17}$$

where $\langle \ldots \rangle$ again denotes an ensemble average or a time average. If the scaling exponent β is chosen to be equal to the diffusion exponent α, the mean value of the distribution of generalized diffusivities asymptotically corresponds to the generalized diffusion coefficient D_α [65].

Anomalous diffusion processes often show weak ergodicity breaking, which means that the ensemble-averaged MSD and the time-averaged MSD do not coincide and the latter becomes a random variable, which varies from one trajectory to another, despite the fact that the corresponding state or phase space of the considered system is not divided into mutually inaccessible regions. The reason for the non-ergodic behavior is a diverging characteristic time scale of the process which means that the measurement time can never be long enough to reach this diverging time scale of the system [65]. The probably most investigated example for such a weakly non-ergodic, anomalous diffusion process is the subdiffusive continuous time random walk (CTRW) [18, 66]. For this CTRW, the distributions of generalized diffusivities which are obtained from ensemble and time averages, respectively, strongly differ. However, analytical formulas for the distributions and their explicit τ-dependence are known [65] and can be used to identify this process in experiments.

The distribution of diffusivities is a new, promising tool for analyzing data from heterogeneous, anisotropic, and anomalous diffusion processes. It characterizes the diffusivity fluctuations along a trajectory or in an ensemble. For instance, it provides simple means for identifying and characterizing anisotropies in the system. An explicit τ-dependence indicates the presence of a complex underlying process, and its analysis characterizes the latter. Its determination is easily accomplished from experimental data.

4 Conclusions

We have investigated experimentally and theoretically the influence of spatially heterogeneous environments and of anisotropies on the diffusive behavior of particles, as well as the question of ergodicity and weak ergodicity breaking, respectively. These questions were addressed via single particle tracking and NMR experiments, which measure time and ensemble averages, respectively. In this way the question of (weak) ergodicity breaking could be addressed. As a tool for the evaluation of these experimental data the concept of the distribution of diffusivities was applied and its properties were elucidated analytically for various model scenarios relevant in this context.

Acknowledgements

The research reported here has been supported by the Deutsche Forschungsgemeinschaft within project P4 “Driven diffusion in nanoscaled materials” of the Saxon Research Group FOR 877 “From Local Constraints to Macroscopic Transport”.

References

[1] L. Venema: *Silicon electronics and beyond*. Nature **479**, 309 (2011)

[2] P. Shemella, S.K. Nayak: *Electronic structure and band-gap modulation of graphene via substrate surface chemistry.* App. Phys. Lett. **94**, 032101 (2009)

[3] F. Lüttich, D. Lehmann, M. Friedrich, Z. Chen, A. Facchetti, C. von Borczyskowski, D.R.T. Zahn, H. Graaf: *Interface properties of OFETs based on an air-stable n-channel perylene tetracarboxylic diimide semiconductor.* phys. stat. sol. A **209**, 585–593 (2012)

[4] L.T. Zhuravlev: *The surface chemistry of amorphous silica. Zhuravlev model.* Colloids and Surfaces A **173**, 1–38 (2000)

[5] V. Dugas, Y. Chevalier: *Surface hydroxylation and silane grafting on fumed and thermal silica*. J. Coll. Interf. Science **264**, 354–361 (2000)

[6] T. Baumgärtel, H. Graaf: *Local anodic oxidation nanolithography on silicon: Chemical routes to functional nanostructures*. In *Lithography: Principles, processes and materials*, ed. T.C. Hennessy, 175–193, Nova Science Publishers (2011)

[7] C. Belgardt, H. Graaf, T. Baumgärtel, C. von Borczyskowski: *Self-assembled monolayers on silicon oxide.* phys. stat. sol. C **7**, 227–230 (2010)

[8] R.K. Iler: *The surface chemistry of silica*. In *The chemistry of silica*, Wiley (1979)

[9] J. Schuster, F. Cichos, J. Wrachtrup, C. von Borczyskowski: *Diffusion of single molecules close to interfaces*. Single Molecules **1**, 299–305 (2000)

[10] J.B. Fleury, O. Claussen, S. Herminghaus, M. Brinkmann, R. Seemann: *Mechanical stability of ordered droplet packings in microfluidic channels.* Appl. Phys. Lett. **99**, 244104 (2010)

[11] R. Wüthrich, E.A. Baranova, H. Bleuler, C. Comninellis: *A phenomenological model for macroscopic deactivation of surface processes.* Electrochemistry Communications **6**, 1199–1205 (2004)

[12] J. Schuster, F. Cichos, C. von Borczyskowski: *Anisotropic diffusion of single molecules in thin liquid films.* Europ. Phys. J. E: Soft Matter and Biological Physics **12**, 75–80 (2003)

[13] M.L. Forcada, C.M. Mate: *Molecular layering during evaporation of ultrathin liquid films.* Nature **363**, 527–529 (1993)

[14] C.J. Yu, A.G. Richter, J. Kmetko, A. Datta, P. Dutta: *X-ray diffraction evidence of ordering in a normal liquid near the solid-liquid interface.* Europhys. Lett. **50**, 487–493 (2000)

[15] D. Täuber: *Characterization of heterogeneous diffusion in confined soft matter.* PhD Thesis, TU Chemnitz (2011)

[16] M.J. Saxton: *Single particle tracking: The distribution of diffusion coefficients.* Biophys. J. **72**, 1744–1753 (1997)

[17] H. Qian, M.P. Sheetz, E.L. Elson: *Single particle tracking. Analysis of diffusion and flow in two-dimensional systems.* Biophys. J. **60**, 910–921 (1991)

[18] A. Lubelski, I.M. Sokolov, J. Klafter: *Nonergodicity mimics inhomogneity in single particle tracking.* Phys. Rev. Lett. **100**, 250602 (2008)

[19] J. Schuster, J. Brabandt, C. von Borczyskowski: *Discrimination of photoblinking and photobleaching on the single molecule level.* J. of Luminesc. **127**, 224–229 (2007)

[20] C. Hellriegel, J. Kirstein, C. Bräuchle, V. Latour, T. Pigot, R. Olivier, S. Lacombe, R. Brown, V.Guieu, C. Payraste, A. Izquiredo, P. Mocho: *Diffusion of single streptocyanine molecules in the nanoporous network of sol-gel glasses.* J. Phys. Chem. B **108**, 14699–14709 (2004)

[21] B. Schulz, D. Täuber, F. Friedriszik, H. Graaf, J. Schuster, C. von Borczyskowski: *Optical detection of heterogeneous single molecule diffusion in thin liquid crystal films.* Phys. Chem. Chem. Phys. **12**, 11555–11564 (2010)

[22] M. Bauer, R. Valiullin, G. Radons, J. Kärger: *How to compare diffusion processes assessed by single-particle tracking and pulsed field gradient nuclear magnetic resonance*. J. Chem. Phys. **135**, 144118 (2011)

[23] S. Krause, P.F. Aramendía, D. Täuber, C. von Borczyskowski: *Freezing single molecule dynamics on interfaces and in polymers.* Phys. Chem. Chem. Phys. **13**, 1754–1761 (2011)

[24] I. Horcas, R. Fernandez, J.M. Gomez-Rodriguez, J. Colchero, J. Gomez-Herrero, A.M. Baro: *WSXM: A software for scanning probe microscopy and a tool for nanotechnology.* Rev. Sci. Instr. **78**, 013705 (2007)

[25] S. Schubert: *Untersuchung der Diffusion und der Anbindung von Farbstoffen an nano-strukturierten Grenzflächen.* Diploma Thesis, TU Chemnitz (2010)

[26] M. Heidernätsch: *Development of a computer program for simulation and analysis of particle movement in thin liquid films.* Master Thesis, TU Chemnitz (2009)

[27] A. Honciuc, A.W. Harant, D.K. Schwartz: *Single molecule observations of surfactant diffusion at the solution-solid interface.* Langmuir **24**, 6562–6566 (2008)

[28] S. Krause, M. Hartmann, I. Kahle, M. Neuman, M. Heidernätsch, S. Spange, C. von Borczyskowski: *Optical tracking of single Ag clusters in nanostructured water films.* J. Phys. Chem. C **117**, 24822–24829 (2013)

[29] S. Krause, M. Heidernätsch, M. Hartmann, C. von Borczyskowski*: Optical investigation of diffusion of single Ag markers in confined water films.* J. Nanopart. Res. **16**, 2700 (2014)

[30] D. Täuber, I. Trenkmann, C. von Borczyskowski: *Influence of van der Waals interactions on morphology and dynamics in ultrathin liquid films at silicon oxide interfaces.* Langmuir **29**, 3583–3593 (2013)

[31] B. Schulz, D. Täuber, J. Schuster, T. Baumgärtel, C. von Borczyskowski*: Influence of mesoscopic structures on single molecule dynamics in thin smectic liquid crystal films.* Soft Matter **7**, 7431–7440 (2011)

[32] D. Täuber, K. Radscheit, R. Camacho, I. Scheblykin, C. von Borczyskowski: *Guest molecule diffusion and conformation influenced by local liquid crystal structure.* diffusion-fundamentals.org **20**, 103 (2013)

[33] D. Täuber, C. von Borczyskowski, M. Schulz: *Fluorescence correlation spectroscopy in thin films at reflecting substrates as a means to study nanoscale structure and dynamics at soft matter interfaces*. submitted to Phys. Rev. E

[34] E. Frey, K. Kroy*: Brownian motion: a paradigm of soft matter and biological physics*. Annalen der Physik **14**, 20–50 (2005)

[35] C. Bräuchle, D.C. Lamb, J. Michaelis*: Single particle tracking and single molecule energy transfer*. Wiley-VCH, Weinheim (2010)

[36] J. Ries, P. Schwille: *Fluorescence correlation spectroscopy.* BioEssays **34**, 361–368 (2012)

[37] M. Hellmann, J. Klafter, D.W. Heermann, M. Weiss: *Challenges in determining anomalous diffusion in crowded fluids.* Journal of Physics-Condensed Matter **23**, 234113 (2011)

[38] F. Feil, S. Naumov, J. Michaelis, R. Valiullin, D. Enke, J. Kärger, C. Bräuchle: *Single-particle and ensemble diffusivities—test of ergodicity.* Angewandte Chemie **124**, 1178–1181 (2012)

[39] A. Shakhov, J. Kärger, R. Valiullin: *Diffusion properties of liquid crystal-based microemulsions*. Colloid and Polymer Science **292**, 1961–1969 (2014)

[40] A. Shakhov, R. Valiullin, J. Kärger: *Tracing molecular propagation in dextran solutions by pulsed field gradient NMR.* Journal of Physical Chemistry Letters **3**, 1854–1857 (2012)

[41] D. Kondrashova, A. Khokhlov, R. Valiullin, J. Kärger: *Propagation of solid-liquid interfaces in disordered linear pores*. diffusion-fundamentals.org **11**, 60 (2009)

[42] D. Kondrashova, M. Dvoyashkin, R. Valiullin: *Structural characterization of porous solids by simultaneously monitoring the low-temperature phase equilibria and diffusion of intrapore fluids using nuclear magnetic resonance.* New Journal of Physics **13**, 015008 (2011)

[43] D. Kondrashova, R. Valiullin: *Freezing and melting transitions under mesoscalic confinement: Application of the Kossel–Stranski crystal-growth model.* The Journal of Physical Chemistry C **119**, 4312–4323 (2015)

[44] J. Szymanski, M. Weiss: *Elucidating the origin of anomalous diffusion in crowded fluids.* Phys. Rev. Lett. **103**, 038102 (2009)

[45] W.S. Price: *NMR studies of translational motion*. University Press, Cambridge (2009)

[46] O.V. Petrov, I. Furó: *NMR cryoporometry: Principles, applications and potential.* Progress in Nuclear Magnetic Resonance Spectroscopy **54**, 97–122 (2009)

[47] J.-H. Jeon, V. Tejedor, S. Burov, E. Barkai, C. Selhuber-Unkel, K. Berg-Sørensen, L. Oddershede, R. Metzler: *In vivo anomalous diffusion and weak ergodicity breaking of lipid granules.* Phys. Rev. Lett. **106**, 048103 (2011)

[48] F. Höfling, T. Franosch: *Anomalous transport in the crowded world of biological cells.* Reports on Progress in Physics **76**, 046602 (2013)

[49] M. Weiss, M. Elsner, F. Kartberg, T. Nilsson: *Anomalous subdiffusion is a measure for cytoplasmic crowding in living cells.* Biophysical Journal **87**, 3518–3524 (2004)

[50] D.S. Banks, C. Fradin: *Anomalous diffusion of proteins due to molecular crowding*. Biophysical Journal **89**, 2960–2971 (2005)

[51] J.P. Bouchaud, A. Georges: *Anomalous diffusion in disordered media – Statistical mechanisms, models and physical applications.* Physics Reports-Review Section of Physics Letters **195**, 127–293 (1990)

[52] R. Valiullin: *Diffusion in nanoporous host systems.* Annual Reports on NMR Spectroscopy **79**, 23–72 (2013)

[53] A. Khokhlov, R. Valiullin: *Mesoporous silicon.* In *Handbook of porous silicon*, ed. L. Canham, Springer International Publishing, pp. 1–12 (2014)

[54] M. Dvoyashkin, A. Khokhlov, R. Valiullin, J. Kärger: *Freezing of fluids in disordered mesopores.* The Journal of Chemical Physics **129**, 154702–154706 (2008)

[55] K.A. Jackson: Kinetic *processes: Crystal growth, diffusion, and phase transitions in materials*. Wiley-VCH, Weinheim (2004)

[56] D. Schneider, R. Valiullin, P.A. Monson: *Filling dynamics of closed end nanocapillaries*. Langmuir **30**, 1290–1294 (2014)

[57] G. Aljaž, V.C. Aleksei, B. Eli, K. Holger, M. Ralf: *Localisation and universal fluctuations in ultraslow diffusion processes.* Journal of Physics A: Mathematical and Theoretical **47**, 492002 (2014)

[58] M. Bauer, M. Heidernätsch, D. Täuber, C. von Borczyskowski, G. Radons: *Investigations of heterogeneous diffusion based on the probability density of scaled squared displacements observed from single molecules in ultra-thin liquid films*. diffusion-fundamentals.org **11**, 104 (2009)

[59] D. Täuber, C. von Borczyskowski: *Single molecule studies on dynamics in liquid crystals*. Int. J. Mol. Sci. **14**, 19506–19525 (2013)

[60] H. Risken: *The Fokker-Planck equation: Methods of solution and applications*. Springer Series in Synergetics **18**, Springer, Berlin, second edition (1989)

[61] M. Heidernätsch, M. Bauer, G. Radons: *Characterizing N-dimensional anisotropic Brownian motion by the distribution of diffusivities*. J. Chem. Phys. **139**, 184105 (2013)

[62] J. Guan, B. Wang, S.C. Bae, S. Granick: *Modular stitching to image single-molecule DNA transport*. J. Am. Chem. Soc. **135**, 6006–6009 (2013)

[63] B. Wang, J. Kuo, S.C. Bae, S. Granick: *When Brownian diffusion is not Gaussian.* Nature Materials **11**, 481–485 (2012)

[64] R. Klages, G. Radons, I.M. Sokolov: *Anomalous transport: Foundations and applications.* Wiley-VCH, Weinheim (2008)

[65] T. Albers, G. Radons: *Subdiffusive continuous time random walks and weak ergodicity breaking analyzed with the distribution of generalized diffusivities.* EPL **102**, 40006 (2013)

[66] G. Bel, E. Barkai: *Weak ergodicity breaking in the continuous-time random walk.* Phys. Rev. Lett. **94**, 240602 (2005)

[67] Y. He, S. Burov, R. Metzler, E. Barkai: *Random time-scale invariant diffusion and transport coefficients.* Phys. Rev. Lett. **101**, 058101 (2008)